Progress In Electromagnetics Research B, Vol. 43, 211–238, 2012

A MACROBASIS FUNCTION MODEL FOR CHARACTERIZING FINITE LARGE-AREA METAMATERIALS

D. Ansari Oghol Beig and H. Mosallaei*

CEM and Photonics Lab., Northeastern University, 409 Dana, 360 Huntington Ave., Boston, MA 02115, USA

Abstract—An acceleration technique for the MoM solution of large-area metamaterial arrays is proposed that relies on numerical extraction of the modal profile associated with the individual array elements followed by projection of the global system equations onto a judiciously constructed reduced solution space. To further enhance the performance of the underlying MoM computations an IE-FFT engine is developed that is adapted for the underlying JMCFIE formulation and higher order quadrilateral discretization. A number of large-area metamaterial arrays are solved and the computational statistics are presented to reflect the advantage of the the proposed methodology.

1. INTRODUCTION

The art of metamaterial design is based on judicious configuration of repeated sub-wavelength sized structures consisting of various materials and geometries often regarded as unit cells or building blocks. Obviously the design relies on our understanding of the physics involved in the function of the building blocks. The design process usually begins with analysis of isolated blocks and proceeds with proper configurations to achieve novel physics. While equivalent bulk properties such as doubly negative material indices are the aim goal, such properties can only be guaranteed through careful design and analysis of the individual and the integrated building blocks. Most recently, large-area metamaterials are finding interesting applications on platforms such as solar cells, aircrafts and planar antenna fixtures, antenna radomes and optical sensors. This, further enhances the need for efficient design tools for such large-area metamaterial arrays. Hence, availability of suitable computational tools is of paramount

Received 21 July 2012, Accepted 20 August 2012, Scheduled 23 August 2012

* Corresponding author: Hossein Mosallaei (hosseinm@ece.neu.edu).

importance to the successful design and analysis of metamaterials. While a large variety of computational methods exist that can potentially address the requirements of metamaterial design, in this work the focus shall remain on method of moments (MoM) and a projection based acceleration of MoM.

Barebone implementation of MoM would clearly be insufficient for any problem of practical interest due to its $\mathcal{O}(N^2)/\mathcal{O}(N^3)$ memory/flops requirement. A variety of (often) interrelated methods have been used to enhance the performance of MoM all of which exploit the low rank nature of the coupling matrices defined between well separated groups of source and observation regions. Examples include fast multipole method (FMM) ($\mathcal{O}(N\log(N))/\mathcal{O}(N\log(N))$) [1], integral equation fast Fourier transform (IE-FFT) ($\mathcal{O}(N^{1.5}\log(N))/\mathcal{O}(N^{1.5}\log(N))$) method [2] and other similar variants most of which are based on the assumption of iterative system matrix solver. Another breed of MoM accelerators are based on solution of a reduced system of equations [3–8]. Such methods will yield $\mathcal{O}(N\log(N))/\mathcal{O}(N\log(N))$ or $\mathcal{O}(N^2)/\mathcal{O}(N^3)$ depending on the choice of an iterative or direct matrix solver. The difficulty with the choice of an iterative solver is the fact that a strong preconditioner might be needed before rapid convergence of the solver can be guaranteed. While the implementation of an efficient preconditioner can be a complicated task, a good preconditioner can also lead to undesirable computational times and memory requirements.

On the other hand, projection methods lead to significant reductions in the effective N, hence allowing for the use of a direct solver and eliminating the need for preconditioners even in the presence of large problems. Moreover, although the use of a direct solver may seem to be computationally more expensive, it significantly reduces the computational cost when the solutions to large number of excitations are required. This is typical to the study of large-area metamaterial problems where the temporal response of the system to a large collection of angles is desired. With these considerations, the current article is based on the choice of a direct solver based projection method.

A projection based acceleration method, as it will be detailed later on, is based on the projection of the system equations onto a reduced vector space and results in often dramatic reductions in the size of the linear system to be solved. Such reduction, from approximation theory point of view, falls into the category of loss compression techniques. Obviously, one must beware that blind application of such compression techniques may lead to undesirable loss of accuracy. In other words, the key to successful implementation of a projection method lies in the

proper generation of the projection space.

Some popular families of projection methods have been around in the computational electromagnetics (CEM) society and have been regarded with different terminologies such as characteristic basis function method (CBFM) [4–8], synthetic basis function method (SBFM) [3] and macro-basis function method (MBFM) [9] owing to the different techniques used in the process of constructing the projection space. These methods, have been applied to the solution of a variety of problems involving non-penetrable, i.e., perfect electric conductor (PEC), and penetrable (dielectric) materials and have been found to be effective particularly when repetition is involved in the problem of interest. Practical examples of such problems include antenna arrays, finite periodic scatterers and two dimensional (2D) and three dimensional (3D) metamaterial array structures. The concept has also been applied to effectively reduce the system matrix obtained from a wire-grid MoM model for plasmonic nanorods [9]. As a continuation to these works, this article focuses on applying a projection method to the surface integral equation (SIE) solution of complex 3D composites made from penetrable dielectric and plasmonic building blocks. As it was mentioned, the key to the successful implementation lies in the proper generation of the projection space and this will be elaborated in detail in Subsection 2.4 and Subsection 2.5. Lastly, some unique physical properties are discussed in Section 3.

2. BRIEF FORMULATION

2.1. Integral Equation Formulation

A variety of integral equation (IE) formulations for penetrable object problems exist in the literature. Most formulations rely on the well known Stratton-Chu field representation formulas [10]. The results reported in this article are obtained using the JMCFIE formulation as it is reflected in (1) [11, 12].

$$\begin{aligned}
&\begin{bmatrix} 1 & \eta_1\hat{n}\times \\ \hat{n}\times & -\eta_1 \end{bmatrix}\begin{bmatrix} -\eta_1\mathcal{L}_1 & \mathcal{K}_1 \\ -\mathcal{K}_1 & -\frac{1}{\eta_1}\mathcal{L}_1 \end{bmatrix}\begin{bmatrix} \mathcal{J} \\ \mathcal{M} \end{bmatrix} \\
&+\begin{bmatrix} -1 & -\eta_2\hat{n}\times \\ -\hat{n}\times & +\eta_2 \end{bmatrix}\begin{bmatrix} -\eta_1\mathcal{L}_2 & \mathcal{K}_2 \\ -\mathcal{K}_2 & -\frac{1}{\eta_2}\mathcal{L}_2 \end{bmatrix}\begin{bmatrix} -\mathcal{J} \\ -\mathcal{M} \end{bmatrix} \\
&= -\begin{bmatrix} 1 & \eta_1\hat{n}\times \\ \hat{n}\times & -\eta_1 \end{bmatrix}\begin{bmatrix} \mathcal{E}_1^{inc} \\ \mathcal{H}_1^{inc} \end{bmatrix}-\begin{bmatrix} -1 & -\eta_2\hat{n}\times \\ -\hat{n}\times & +\eta_2 \end{bmatrix}\begin{bmatrix} \mathcal{E}_2^{inc} \\ \mathcal{H}_2^{inc} \end{bmatrix}
\end{aligned} \tag{1}$$

In (1), $\mathcal{J}$ and M represent the equivalent electrical and magnetic surface currents on the material interface separating two homogeneous

material regions while $\mathcal{E}_i^{inc}$ and $\mathcal{H}_i^{inc}$ stand for the incident fields in region i. At the same time, $\mathcal{L}$ and $\mathcal{K}$ are the integral operators used in the field representation formulas and are defined in (2) and (3).

$$\mathcal{E} = -\jmath\eta k\int_S \mathcal{J}(r')\, g(|r-r'|)\, dS' + \jmath\frac{\eta}{k}\nabla\int_S \mathcal{J}\,(r')\cdot\nabla' g(|r-r'|)\, dS' \quad (2)$$

$$\mathcal{K}(\mathcal{J}) := \int_S \nabla' g\,(|r-r'|)\times\mathcal{J}\,(r')\, dS' \quad (3)$$

2.2. Discretization

The integral equation formulation of Subsection 2.1 needs to be discretized to yield a linear system of equations before it can be solved on a digital computer. This is achieved via a discretization of the geometry followed by assignment of a set of basis functions and a Galerkin trial and testing procedure [11, 12]. The implementation details of the process are well beyond the scope of this article and such techniques are well documented in CEM literature. Here, we suffice to mention that in all our examples a mesh of curvilinear quadrilateral elements along with hierarchical divergence conforming basis functions has been used [13]. Also, since a critical part of such implementation lies in the proper evaluation of the singular integrals associated with the IE operators we hint that an adaptive quadrature method along with proper singularity treatment has been implemented based on [14].

2.3. Vector Space Reduction

The CBFM and the SBFM are probably the two most popular projection based methods reported in electrical engineering literature. Details of these projection methods can be found in numerous articles [3–9] and we shall not repeat what is already documented in the literature. For the sake of consistency we suffice to mention that the original MoM system of equations has the form $Z_{NxN}X_{N\times 1} = Y_{N\times 1}$ where Z is the system (impedance) matrix while X and Y respectively denote the solution and the right hand side vectors. Instead of solving $ZX = Y$, one can seek an approximate solution by projecting the problem onto a reduced vector space spanned by $U = [X_1, X_2, \ldots, X_n]_{N\times n}$ by solving $(U^T ZU)_{n\times n}x_{n\times 1} = U^T_{n\times N}Y_{N\times 1}$ and substituting $X = Ux$ afterwards. The solution X obtained in this fashion is an approximate solution to the original $N \times N$ problem and its accuracy depends on the proper choice of the projection space $\{X_1, X_2, \ldots, X_n\}$. As it will be explained in the next section, the discrete nature of the building blocks is exploited for efficient construction of the projection space. However, it must be noted

that similar techniques can be applied to problems with continuous geometries as it has been reported in [4, 6, 7].

2.4. Projection Space

The unknowns in a metamaterial problem can be grouped in accordance to the individual building blocks. Consider a 2×1 array as depicted in Figure 1, the resulting linear problem may be written as:

$$\begin{bmatrix} Z_{11} & Z_{12} \\ Z_{21} & Z_{22} \end{bmatrix} \begin{bmatrix} I_1 \\ I_2 \end{bmatrix} = \begin{bmatrix} F_1 \\ F_2 \end{bmatrix} \tag{4}$$

The grouping of the problem unknowns as it is reflected in (4) becomes a necessity in the way the projection spaces are constructed in this work. The process for the generation of the projection space can be itemized as follows:

i) Excite the individual blokes by various excitations, i.e., different plane-waves or near field sources and populate the list of solutions due to these excitations.

ii) Perform a truncated singular value decomposition (SVD) on the above-mentioned population of individual block solutions. The SVD guarantees linear independence of the resulting spanning vectors and provides a means for controlling the size of the projection space and the resulting reduction in problem unknowns.

It is worth mentioning that when identical building blocks are used in the array, the above process needs to be performed only once, hence resulting in significant reduction in the computational cost.

2.5. The Pool of Block Excitations and Block Solutions

As mentioned in the previous section, a pool of solutions needs to be generated for the individual building blocks. It is of paramount importance for the pool of block solutions to be able to efficiently

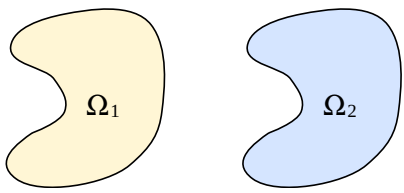

Figure 1. Partition of the array problem DoF in accordance to the building blocks.

reproduce the actual array solution. In other words, the resulting projection space must simultaneously satisfy two requirements:

i) Be as small as possible.

ii) Be able to accurately reproduce the final solution of the individual blocks as they appear in the actual array.

It is not easy to devise a general mathematical recipe that meets the above-mentioned requirements regardless of the geometry and the structure of the problem at hand. This is where physical intuition and engineering experience can be incorporated into the problem solution. It is understood that the solution of an individual block , as it appears in the array problem, is a response to the interaction of the block with the primary excitation as well as the secondary, the tertiary and the other higher order sources particularly those in a close neighborhood of the block. Hence, inspired by the Huygens principle and considering the array nature of the metamaterial problem, the following approach is proposed for the generation of the desired pool of block solutions.

i) Excite the building block by means of a properly distributed spectrum of plane waves and the associated solutions. These are often regarded as the primary solutions [6].

ii) Excite the building block by induced currents on its neighbors due to excitations mentioned in item i) . These will be regarded as the secondary solutions.

iii) Excite the building block by induced currents on its neighbors due to excitations mentioned in item ii) . These will be regarded as the tertiary solutions.

The above list can be extended to include quaternary, quinary and other higher order effects. However, it is our experience that solutions up the secondary level will be sufficient for the generation of the desired projection space for the problems encountered in this work. Figure 2 schematically depicts the process by means of which the primary, the secondary and the ternary solutions are generated followed by an SVD truncation for the purpose of generating the block projection matrix U_1.

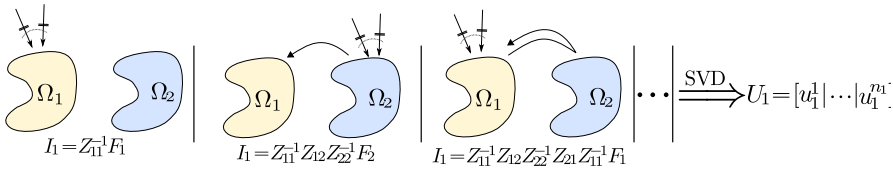

Figure 2. Schematic visualization of the macrobasis function generation process.

2.6. Array Redundancies

In metamaterial design, the interest in the solution of large finite arrays stems from the need to obtain material properties from the operation of large clusters of building blocks. Hence, it is important to exploit the existing redundancies in the arrays.

Suppose an array of $N_x \times N_y \times N_z$ identical building blocks is given and suppose that each building block is associated with n unknowns. It is clear that $N_x N_y N_z n$ unknowns are involved in the problem and that $N_x^2 N_y^2 N_z^2$ block matrices should be calculated, which is in $\mathcal{O}(N^2)$ proportion to the number of problem unknowns if a direct MoM formalism is adopted. However, if identical building blocks are used across the array, the couplings in the array can be classified according to the array displacement between individual blocks. For example, as it is shown in Figure 3, the coupling block required for coupling a block to its immediate neighbour on the right, i.e., Z_{12}, occurred twelve times across the 4×4 array while the coupling block responsible for coupling a block to a block two steps on the right occurred eight times in the 4×4 array of Figure 3. Considering these redundancies the number of block matrices that need to be calculated reduces to $(2N_x+1)(2N_y+1)(2N_z+1)$ which is in linear proportion to the number of unknowns in the problem (note that the Z_{ij} block would be different from the Z_{ji} block).

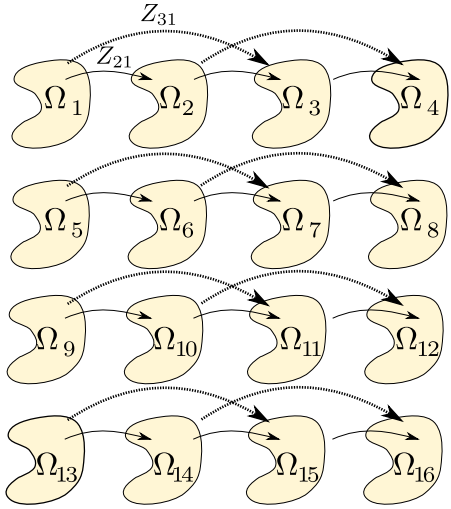

Figure 3. Array redundancies listed for block coupling matrices Z_{21} and Z_{31}.

2.7. IE-FFT Acceleration of Far-field Interactions

As discussed in Subsection 2.6, the coupling blocks in the global matrix can be classified in accordance to the respective distance and orientation of the coupling on the array and the same concept applies to the reduced version of these blocks. On the other hand, the generation of the reduced coupling blocks requires the application of the non reduced matrix blocks on the collection of MBFs. In this work, except for the coupling blocks that correspond to near neighbour to neighbour interactions, a variant of the IE-FFT accelerated MoM matrix-vector multiplier [2] and has been implemented. The implementation details of the accelerator are beyond this article but we suffice to mention that the method has been adapted for efficient operation on arrays and has been extended to include the integral operators involved in the JMCFIE formulation for penetrable objects.

3. NUMERICAL RESULTS

The results of the proposed macrobasis approach are reported in the following sections and cover a number of dielectric and plasmonic metamaterials. As a sanity check, the preceding two examples include comparisons against direct MoM solutions. It is our experience that far field quantities such as radiation pattern can hide potentially existing inaccuracies in near field results. Hence, for the sake of stronger verification we have chosen to study the frequency response of the surface tangent field energies, i.e., $\int_S \parallel \hat{n} \times \mathcal{E} \times \hat{n} \parallel^2 dS$ and $\eta_0 \int_S \parallel \hat{n} \times \mathcal{H} \times \hat{n} \parallel^2 dS$. Note that the term energy is here used in the mathematical sense. Both dielectric and plasmonic materials

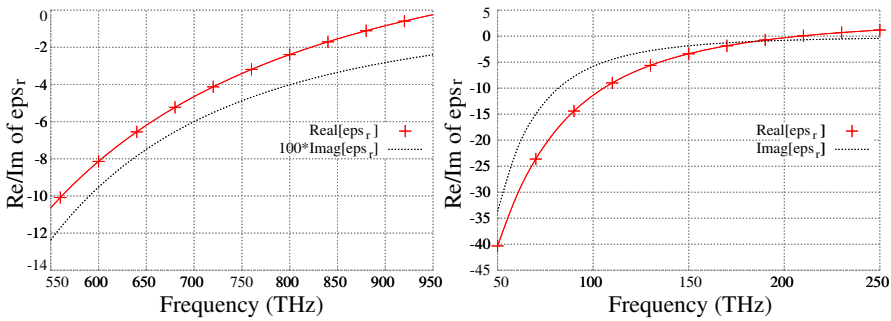

Figure 4. The Drude model characterization of the real and imaginary parts of the relative dielectric constant for (a) silver and (b) ITO.

are present in our examples. The plasmonic material used in the presented examples is either silver or indium tin oxide (ITO). For these materials, a Drude characterization compatible with that of [15] is used in accordance to which the actual dielectric constants have been plotted in Figure 4.

It is necessary to clarify that due to the limitations of human eye and computer graphics we have decided to crop the near field plots (for the 40×40 arrays) into the 5×5 central part of the array. All surface plots visualize either the electrical or the magnetic field on the surface of the scatterer. Each MBFs, as it occurs in the MoM formulation, represents an electrical and a magnetic current distribution, i.e., $\mathcal{J}$ and $\mathcal{M}$. However, these can be easily converted to scattered fields $\mathcal{E}$ and $\mathcal{H}$ through $\mathcal{H} = \mathcal{J} \times \hat{n}$ and $\mathcal{E} = \hat{n} \times \mathcal{M}$. Hence, we have chosen to visualize $\mathcal{E}$ and $\mathcal{H}$ in all figures including scattered field plots and MBF plots. Lastly, one must note that all figures have the same 3D view angle and the orientation of the x, y, and z axes is consistent to the elaboration of Figure 7(b).

Last but not least, some computational statistics are reported in this article and compared against those of the commercial solver, CST. Nevertheless, note that a one-to-one comparison (specially on memory usage) will not be logical simply because CST's results are obtained using an iterative solver while the present method is based on a direct solver. Also, these statistics are for the problem solution at a single frequency point.

3.1. Dielectric Spheroid

The first example discussed here consist of a planar array of dielectric spheroids with radius of 36 nm and a dielectric constant of $\epsilon_r = 30$. The lattice constant, i.e., the center to center spacing of the array elements, is 150 nm. The structure becomes resonant at around 745 THz as it can be seen from the frequency responses in Figure 5 which is in agreement to what is obtained by means of Mie theory [16]. Figure 5(a) studies the agreement between MoM and the proposed macrobasis approach for the solution of a 5×5 array. This is followed by the frequency responses for the 40×40 array obtained by means of the proposed method in Figure 5(b).

Figure 6 lists the first six macrobasis functions obtained using the methodology discussed in Subsection 2.4 and Subsection 2.5. In Figure 6 one observes that the first three modes consist of pure magnetic dipoles, i.e., $\mathcal{H}_0$ through $\mathcal{H}_2$ followed by an electric dipole and another two mixed modes. In [17, 18], it is mentioned that the first resonance of dielectric sphere is a magnetic dipole mode while the second one is an electric dipole mode and other higher order

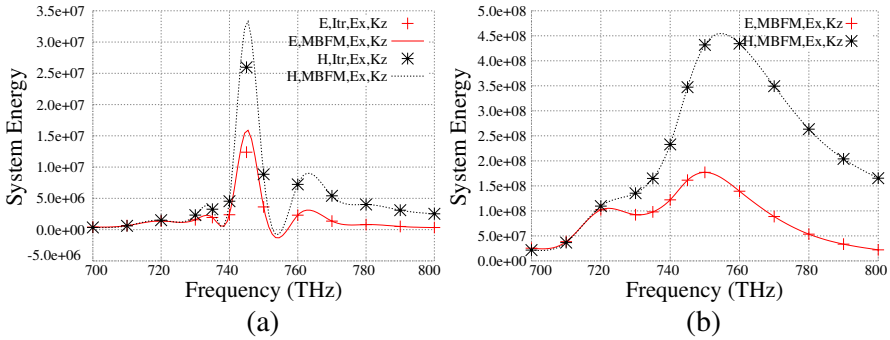

Figure 5. Dielectric spheroid. The frequency response of the surface field energy in response to $\mathcal{E} = \hat{x}e^{-\jmath k_0 \hat{z}\cdot\vec{r}}$. MBFM and Itr respectively refer to MBFM and iterative MoM. The E and H in the legends respectively refer to the electrical and magnetic surface energies. At the same time E_x and K_z indicate that the incident wave is polarized along $\hat{x}$ and propagates along $\hat{z}$. (a) Comparing MBFM results to iterative MoM for 5×5 array. (b) MBFM results for 40×40 array.

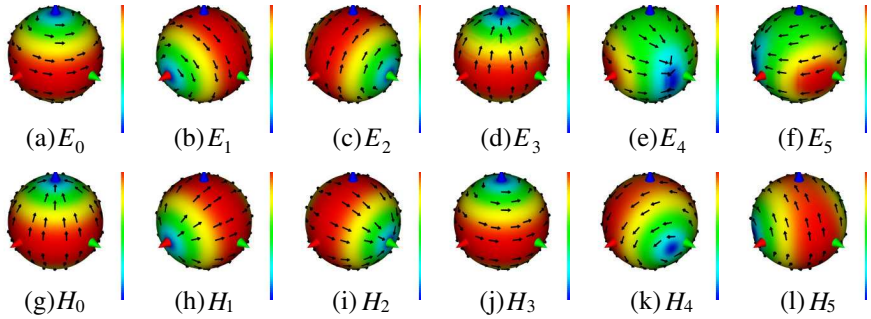

Figure 6. Dielectric spheroid. The real part of the tangential field due to the first six MBFs generated for the array at $f = 745\,\text{THz}$. The $\mathcal{E}_i$ and the $\mathcal{H}_i$ captions signify electrical and magnetic field representation of the ith MBF.

modes follow afterwards. The macrobasis plots presented here clearly demonstrate the same concept. The near field results at the resonance ($f = 745\,\text{THz}$) are plotted in Figures 7, 8, 9 and 10, from which one observes the similarity between the field on the central element(s) with that of the third macrobasis function depicted in Figures 6(c) and 6(i).

The unit cell in this problem was discretized with 96 curvilinear quadrilateral elements supporting a total of 3840 unknowns. This, for

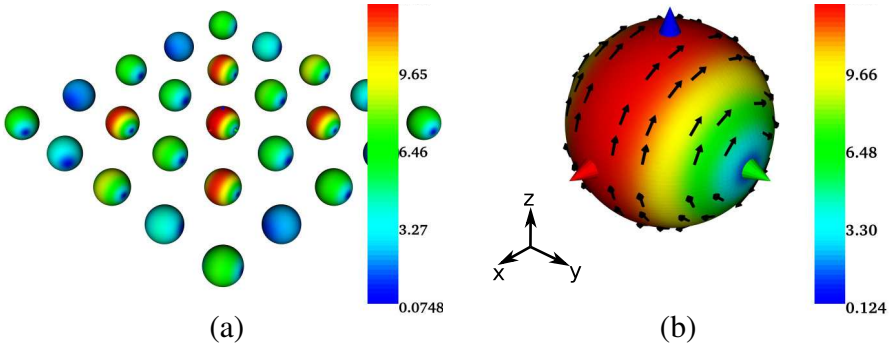

Figure 7. Dielectric spheroid. Real part of the solution of the tangential field 5×5 array at $f = 745$ THz in response to $\mathcal{E} = \hat{x}e^{-\jmath k_0 \hat{z}\cdot\vec{r}}$. $\mathcal{E}/\mathcal{H}$ signifies the tangential electric/magnetic field. (a) $\mathcal{E}$. (b) $\mathcal{E}$ on the central element.

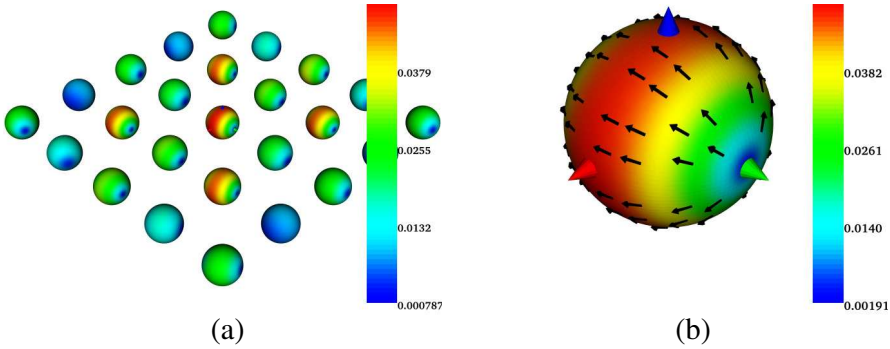

Figure 8. Dielectric spheroid. Real part of the solution of the tangential field 5×5 array at $f = 745$ THz in response to $\mathcal{E} = \hat{x}e^{-\jmath k_0 \hat{z}\cdot\vec{r}}$. $\mathcal{E}/\mathcal{H}$ signifies the tangential electric/magnetic field. (a) $\mathcal{H}$. (b) $\mathcal{H}$ on the central element.

the 40×40 array leads to a total of 6.144 million unknowns. The computational statistics for $f = 700$ THz are reflected in Table 1. For other frequencies, the number of MBFs is less than or equal to that of $f = 700$ THz and hence the statistics in Table 1 reflect the worst case scenario for the dielectric spheroid problem. All of the computational statistics reported Table 1 were obtained on a dual Intel Xeon workstation. However, all parts of the computation were carried out using a single thread ignoring the parallel capabilities of the workstation. Obviously, much better times can be obtained if an efficient parallelization is carried. Note that all computations are carried out in double precision floating point arithmetics while the

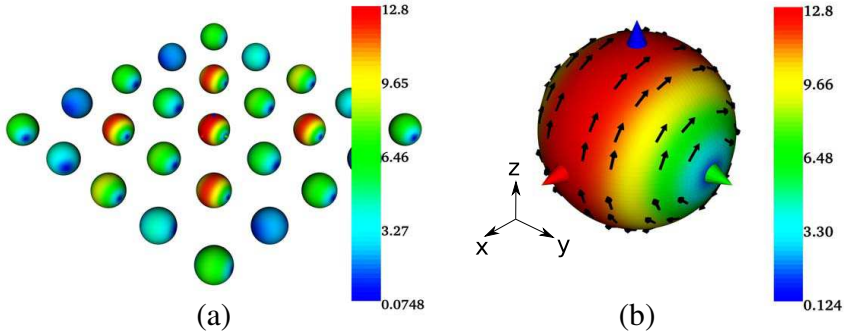

Figure 9. Dielectric spheroid. Real part of the tangential field solution of the 40×40 array at $f = 745\,\text{THz}$ in response to $\mathcal{E} = \hat{x}e^{-\jmath k_0 \hat{z}\cdot\vec{r}}$. $\mathcal{E}/\mathcal{H}$ signifies the tangential electric/magnetic field.

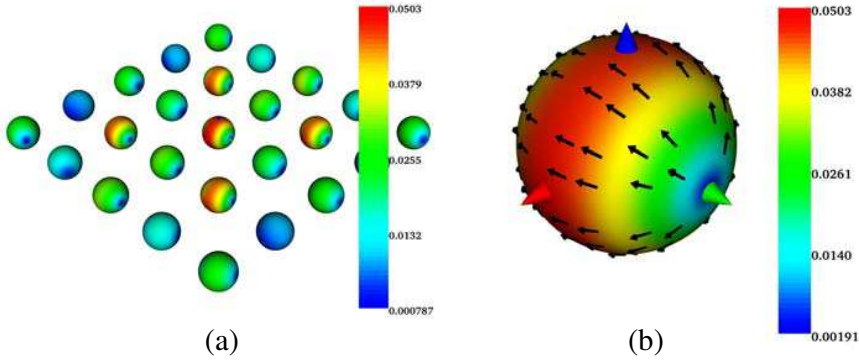

Figure 10. Dielectric spheroid. Real part of the tangential field solution of the 40×40 array at $f = 745\,\text{THz}$ in response to $\mathcal{E} = \hat{x}e^{-\jmath k_0 \hat{z}\cdot\vec{r}}$. $\mathcal{E}/\mathcal{H}$ signifies the tangential electric/magnetic field.

data reported for CST is based on a single precision floating point arithmetics. Thus, for any meaningful comparison with CST, CST memory usage and CPU times must be scaled accordingly. Hence, from Table 1, it is clear that the proposed MBF approach can be very efficient for the analysis of large-area metamaterial arrays. As such, our model can provide a fast and accurate analysis for the performance characterization of large metamaterial arrays. In addition, the method allows for direct observation of the modal profile associated with the

Table 1. Computational statistics for the dielectric spheroid problem at $f = 700\,\text{THz}$. In the first part, from left to right, the table lists: Array dimensions, number of quadrilateral elements, total number of DoF, IE-FFT time spent on calculation of reduced far field blocks, computation time for near field integrals, MBFS' SVD threshold, number of MBFs, computation time for MBFS, LU factorization time for the reduced global matrix and peak memory usage dictated by the reduce global matrix plus other overheads. The second part lists CST statistics for the 10×10 array.

MBFM (double precision)

Dim.	Elements	DoF	IE-FFT	NF	MBF (T/N/time)	LU	Peak Mem.
1×1	96	3840	23 s	5221 s	0.025/16/183 s	0.01 s	4096B+0.7GB
10×10	9.6 K	384 K	111 s	5221 s	0.025/16/183 s	0.8 s	39.06MB+1.GB
40×40	153.6 K	6.144 M	1832 s	5221 s	0.025/16/183 s	3721 s	9.76GB+1.2GB

CST (single precision)

Dim.	Elements	DoF	CPU Time	Peak Mem.
10×10	83.6 K	250.8 K	33587 s	21.01 GB

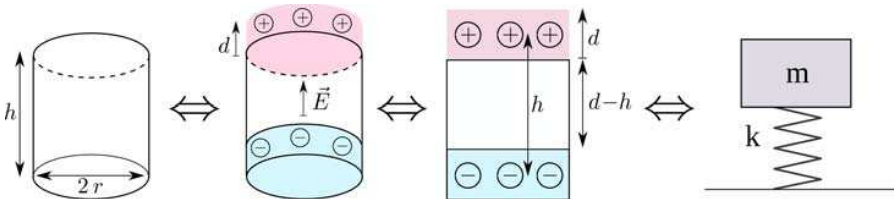

Figure 11. A mass-spring analogy to plasmonic resonance.

building blocks of the system. This, in return, allows for a more intuitive tailoring of the intended physical properties of metamaterials.

3.2. Plasmonic Spheroid

This example shares the same geometry and dimensions with that of the dielectric spheroid of previous section. The difference here is that the spheroids are made from silver which, according to the Drude model, behaves as a plasmonic material having a negative dielectric constant. In [19], it has been documented that the resonant frequency of plasmonic particles can be associated with aspect ratio of the particle along the direction of the polarization of the incident electrical field. Considering the Columbian nature of the electrostatic

forces and assuming that ρ_m and ρ_e are the mass and charge density of the free charge carriers in the particle system depicted in Figure 11, an analogy can be drawn between the stiffness k of the mass-spring system and $\rho_e^2 A^2/h = \rho_e^2 \pi^2 r^4/h$ as a stiffness parameter of the plasmonic particle while the mass of the free charge carriers can be approximated by $\rho_m Ah = \rho_m \pi r^2 h$. Hence, using a mass and spring analogy, the resonance of the system should occur at $\omega_r^2 = \frac{\rho_e^2 A}{\rho_m h^2} = \frac{\rho_e^2 \pi r^2}{\rho_m h^2} \propto r/h$ [20]. Hence, the electro-mechanical nature of the plasmonic resonance explains why it can be at achieved with sub-wavelength structures while it is revealed that the aspect ratio of the particle along the incident polarization axis is a main driving factor that determines the frequency of the resonance.

As it can be seen from the frequency responses in Figure 5, the plasmonic array becomes resonant at around 837 THz. This is of course in agreement with Mie theory [16] predictions. Figure 12(a) studies the agreement between MoM and the proposed macrobasis approach for the solution of a 5×5 array. This is followed by the frequency response for the 40×40 array obtained by means of the proposed method in Figure 12(b).

Figure 13 lists the first six macrobasis functions associated with the plasmonic array. As can be seen, the modes here begin with

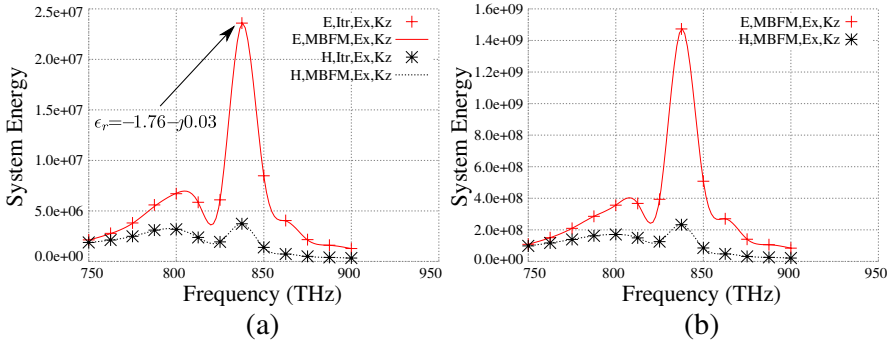

Figure 12. Plasmonic spheroid. The frequency response of the surface field energy in response to $\mathcal{E} = \hat{x}e^{-\jmath k_0 \hat{z}\cdot\vec{r}}$. MBFM and Itr respectively refer to MBFM and iterative MoM. The E and H in the legends respectively refer to the electrical and magnetic surface energies. At the same time E_x and K_z indicate that the incident wave was polarized along $\hat{x}$ and propagated along $\hat{z}$. The arrow pointing to the peak of the curve indicates the actual value of the plasmonic ϵ_r at the resonance frequency. (a) Comparing MBFM results to iterative MoM for 5×5 array. (b) MBFM result for 40×40 array.

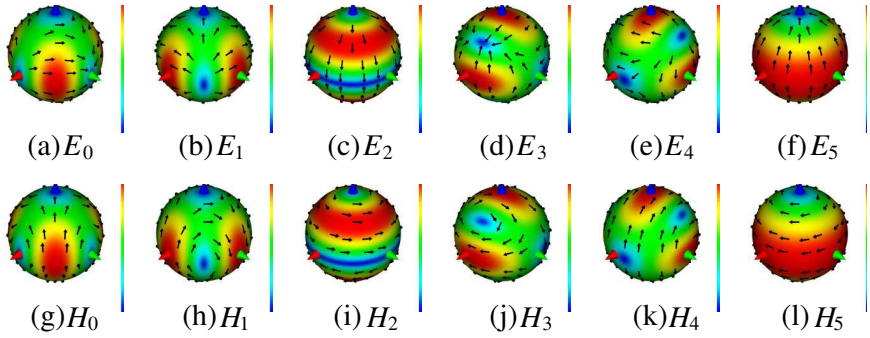

Figure 13. Plasmonic spheroid. The real part of the tangential field due to the first six MBFs generated for the array at $f = 837.5\,\text{THz}$. The $\mathcal{E}_i$ and the $\mathcal{H}_i$ captions signify electrical and magnetic field representation of the ith MBF.

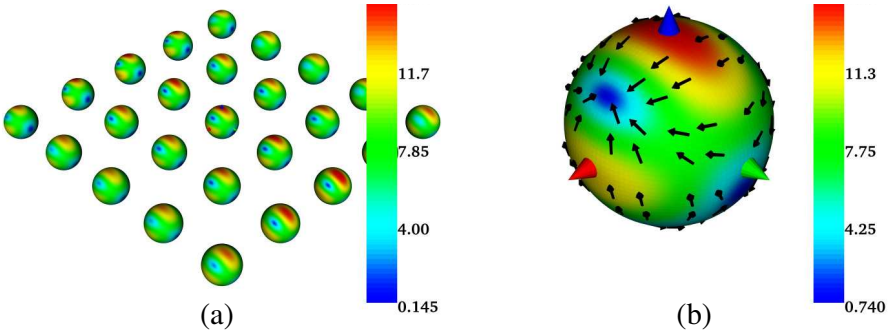

Figure 14. Plasmonic spheroid. Real part of the tangential field solution of the 5×5 array at $f = 837.5\,\text{THz}$ in response to $\mathcal{E} = \hat{x}e^{-\jmath k_0 \hat{z}\cdot\vec{r}}$. $\mathcal{E}/\mathcal{H}$ signifies the tangential electric/magnetic field. (a) $\mathcal{E}$. (b) $\mathcal{E}$ on the central element.

distributions that are more like quadrupoles while the dipolar modes occur further down in the sixth macrobasis function and afterwards. The first and the sixth mode are dielectric dipole modes as one expects from the analysis of isolated plasmonic particles. However, as it can been seen here, strong interactions have occurred between the array elements exciting the higher order modes resulting in a mixed mode profile. The near field results are plotted in Figure 14, Figure 15, Figure 16 and Figure 17 where one immediately observes the similarity between the field on the central element(s) with that of the third macrobasis function depicted in Figure 6(d) and Figure 6(j).

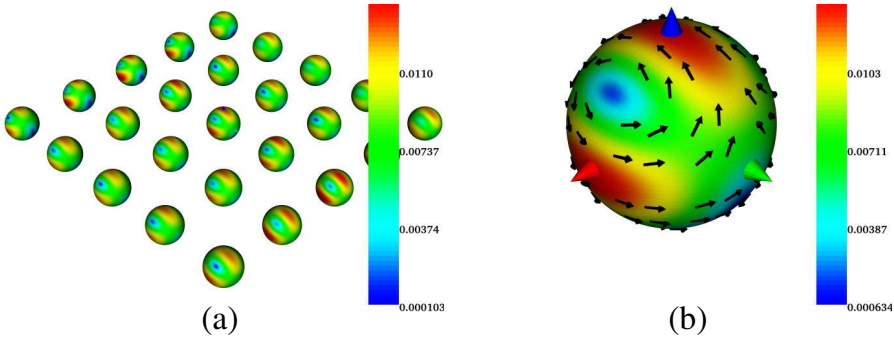

Figure 15. Plasmonic spheroid. Real part of the tangential field solution of the 5×5 array at $f = 837.5\,\text{THz}$ in response to $\mathcal{E} = \hat{x}e^{-\jmath k_0 \hat{z}\cdot\vec{r}}$. $\mathcal{E}/\mathcal{H}$ signifies the tangential electric/magnetic field. (a) $\mathcal{H}$. (b) $\mathcal{H}$ on the central element.

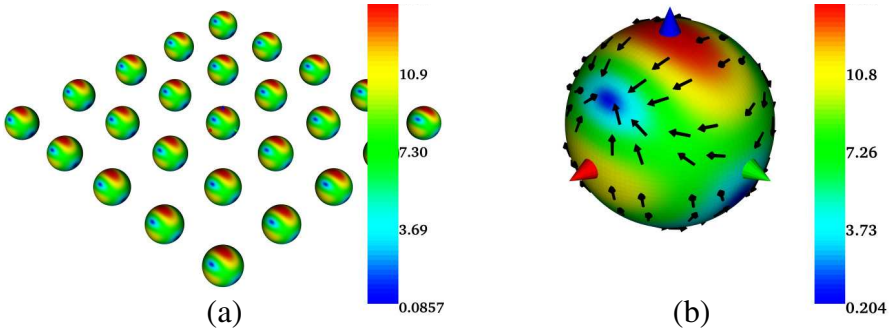

Figure 16. Plasmonic spheroid. Real part of the tangential field solution of the 40×40 array at $f = 837.5\,\text{THz}$ in response to $\mathcal{E} = \hat{x}e^{-\jmath k_0 \hat{z}\cdot\vec{r}}$. $\mathcal{E}/\mathcal{H}$ signifies the tangential electric/magnetic field. (a) $\mathcal{E}$ on the central 5×5 section. (b) $\mathcal{E}$ on the central element.

The two examples presented in Subsection 3.2 and Subsection 3.1 demonstrate the ability of our model in fast and accurate prediction of the behaviour and the physics of metamaterial arrays.

3.3. Plasmonic Ellipsoid

A quick glance at the results of Figure 5(b) and Figure 12(b) reveals that the resonance occurring in Figure 5(b) is magnetically dominant while the resonance occurring in Figure 12(b) is more of electrical nature. In metamaterial design, it is often a necessity to obtain various kinds of resonances at given frequencies. One way to achieve this

with plasmonic particles, is to control the effective aspect ratio of the resonant building blocks. In [19], the controllability of the plasmonic resonances based on the aspect ratio of the particle with respect to the incident field has been discussed. To further demonstrate this effect, a plasmonic ellipsoid with axis dimensions of $a_x = 32\,\text{nm}$, $a_y = 20\,\text{nm}$ and $a_z = 20\,\text{nm}$ is considered as the building block of the array. The lattice constant d equals to 150 nm and the structure is excited by plane waves propagating along z axis. To demonstrate the effect of the aspect ratio versus polarization, plane wave with two different polarizations,

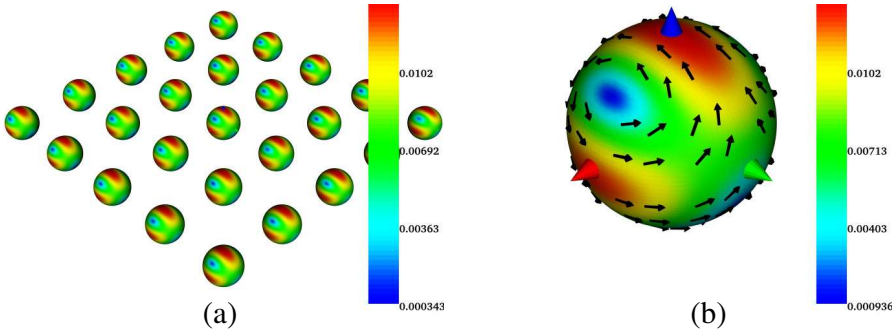

Figure 17. Plasmonic spheroid. Real part of the tangential field solution of the 40×40 array at $f = 837.5\,\text{THz}$ in response to $\mathcal{E} = \hat{x}e^{-\jmath k_0 \hat{z}\cdot\vec{r}}$. $\mathcal{E}/\mathcal{H}$ signifies the tangential electric/magnetic field. (a) $\mathcal{H}$ on the central 5×5 section. (b) $\mathcal{H}$ on the central element.

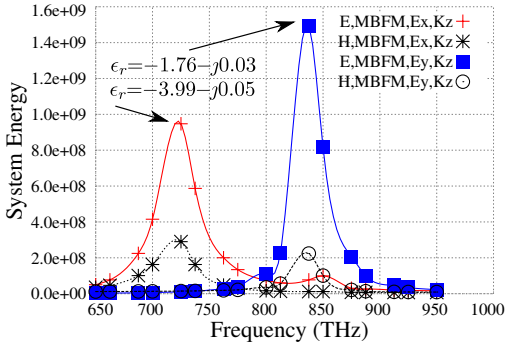

Figure 18. Plasmonic ellipsoid. The frequency response of the surface field energy on the 40×40 array in response to $\mathcal{E} = \hat{x}e^{-\jmath k_0 \hat{z}\cdot\vec{r}}$ and $\mathcal{E} = \hat{y}e^{-\jmath k_0 \hat{z}\cdot\vec{r}}$. The E_x and E_y and K_z in the legend corresponds to the polarization and propagation direction of the incident fields. The arrow pointing to the peak of the curves indicates the actual value of the plasmonic ϵ_r at the resonance frequencies.

i.e., $\hat{x}$ and $\hat{y}$, are considered.

Evident from Figure 18 is that with $\hat{x}$ polarized incident field the resonance shifts down 725 THz while with a $\hat{y}$ polarized incident field the resonance occurs at around 837.5 THz. At both 725 THz and 827.5 THz the dominant macrobasis functions begin electrical dipoles as one can observe from Figure 19 and Figure 20. Again, the near field plots are given Figure 21, Figure 22, Figure 23 and Figure 24. Comparing Figure 21 and Figure 22 with Figure 19 indicates that the resonance at 725 THZ is dominated by the first electrical dipole mode listed in Figure 19. A similar conclusion can be made by comparing Figure 23 and Figure 24 with Figure 20.

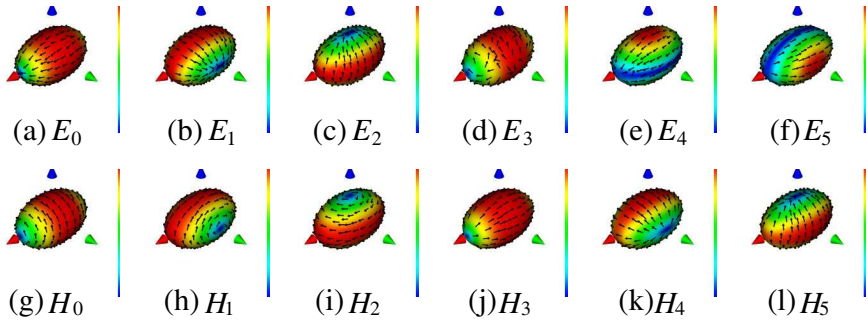

Figure 19. Plasmonic ellipsoid. The real part of the tangential field due to the first six MBFs generated for the array at $f = 725$ THz. The $\mathcal{E}_i$ and the $\mathcal{H}_i$ captions signify electrical and magnetic field representation of the ith MBF.

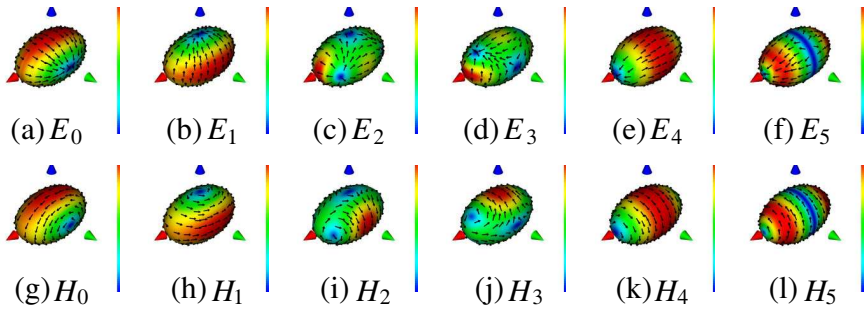

Figure 20. Plasmonic ellipsoid. The real part of the tangential field due to the first six MBFs generated for the array at $f = 837.5$ THz. The $\mathcal{E}_i$ and the $\mathcal{H}_i$ captions signify electrical and magnetic field representation of the ith MBF.

3.4. Core-shell

So far we have considered examples consisting of a pure dielectric or plasmonic building block and we have observed that these structures can exhibit electrically or magnetically dominant resonances at certain frequencies. Nevertheless, in metamaterial design, doubly negative materials can be realized by means of structures that exhibit simultaneous electrical and magnetic resonances. A typical example of such structures is the core-shell consisting of a dielectric spheroidal core coated with certain thickness of a plasmonic material. It can

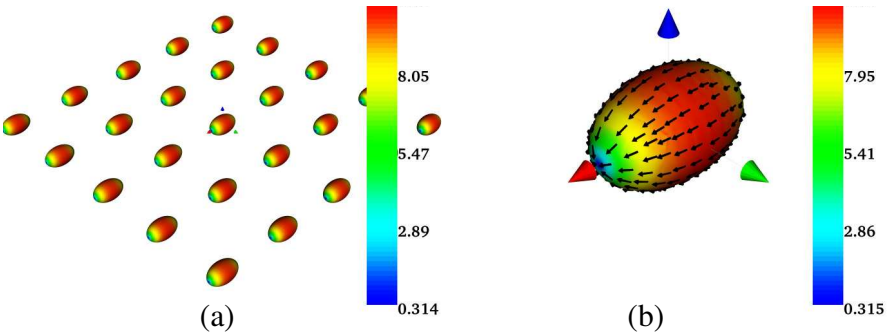

Figure 21. Plasmonic ellipsoid. Real part of the tangential field solution of the 40×40 array in response to $\mathcal{E} = \hat{x}e^{-\jmath k_0 \hat{z}\cdot\vec{r}}$ at 725 THz. $\mathcal{E}/\mathcal{H}$ signifies the tangential electric/magnetic field. (a) $\mathcal{E}$ on the central 5×5 section. (b) $\mathcal{E}$ on the central element.

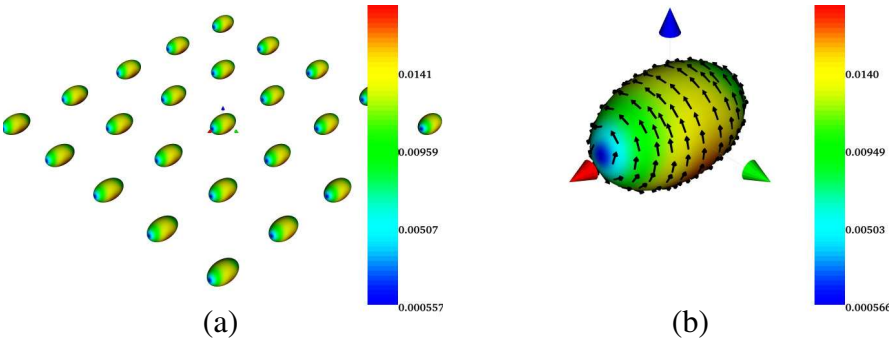

Figure 22. Plasmonic ellipsoid. Real part of the tangential field solution of the 40×40 array in response to $\mathcal{E} = \hat{x}e^{-\jmath k_0 \hat{z}\cdot\vec{r}}$ at 725 THz. $\mathcal{E}/\mathcal{H}$ signifies the tangential electric/magnetic field. (a) $\mathcal{H}$ on the central 5×5 section. (b) $\mathcal{H}$ on the central element.

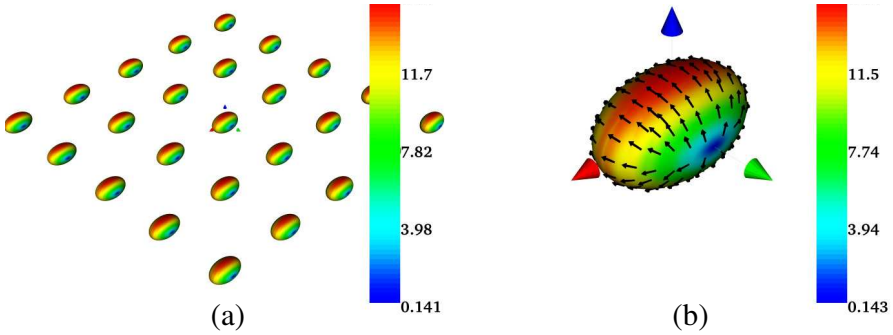

Figure 23. Plasmonic ellipsoid. Real part of the tangential field solution of the 40×40 array in response to $\mathcal{E} = \hat{y}e^{-\jmath k_0 \hat{z}\cdot\vec{r}}$ at 837.5 THz. $\mathcal{E}/\mathcal{H}$ signifies the tangential electric/magnetic field. (a) $\mathcal{E}$ on the central 5×5 section. (b) $\mathcal{E}$ on the central element.

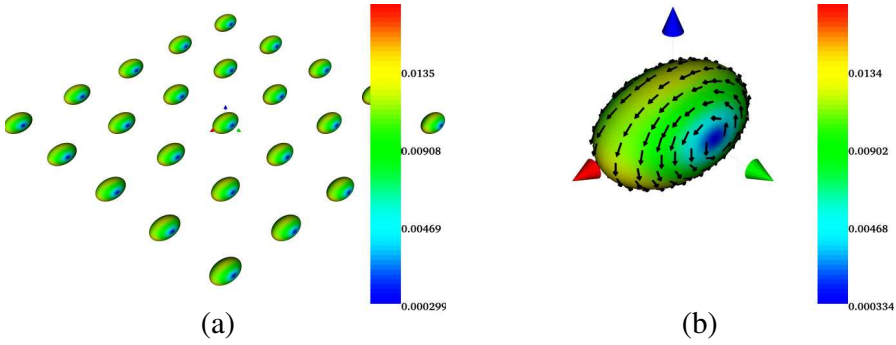

Figure 24. Plasmonic ellipsoid. Real part of the tangential field solution of the 40×40 array in response to $\mathcal{E} = \hat{y}e^{-\jmath k_0 \hat{z}\cdot\vec{r}}$ at 837.5 THz. $\mathcal{E}/\mathcal{H}$ signifies the tangential electric/magnetic field. (a) $\mathcal{H}$ on the central 5×5 section. (b) $\mathcal{H}$ on the central element.

be shown that such structures can exhibit double negative (DNG) material properties. The core-shell structure discussed here is designed to exhibit simultaneous electric and magnetic resonance at around 195 THz. Thus, with an ITO plasmonic shell and a dielectric core with a dielectric constant of $\epsilon_r = 20$, the radius of the core is determined to be 172.5 nm while the outer radius of the shell is determined to be 225 nm. The lattice constant in this case is chosen to be equals to 1000 nm and the dielectric constant of the ITO shell is characterized via an appropriate Drude model as it has been discussed in Section 3 and depicted in Figure 4(b).

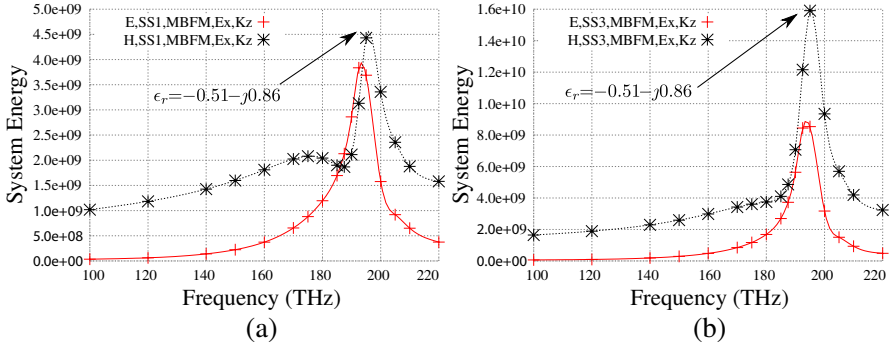

Figure 25. Core-shell. The frequency response of the surface field energy on the 40×40 array in response to $\mathcal{E} = \hat{x}e^{-\jmath k_0 \hat{z}\cdot\vec{r}}$. The E_x and K_z in the legend signify the polarization and propagation direction of the incident field. The arrow pointing to the peak of the curve indicates the actual value of the plasmonic ϵ_r at the resonance frequency. (a) Shell. (b) Core.

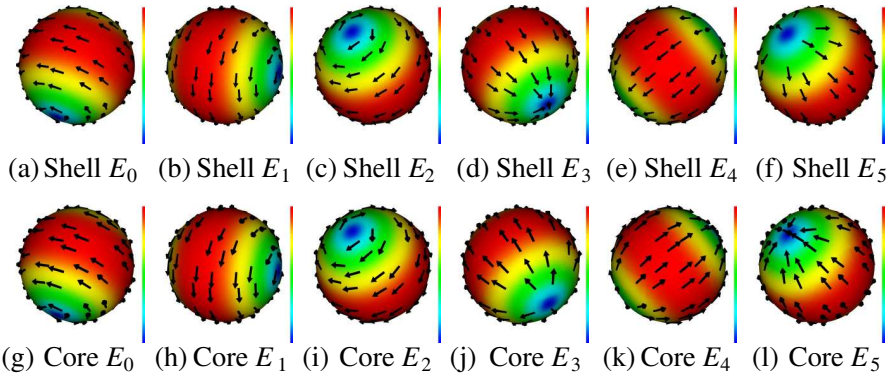

Figure 26. Core-shell. The real part of the tangential electric field due to the first six MBFs generated for the array at $f = 190$ THz. The $\mathcal{E}_i$ captions signify electrical and magnetic field representation of the ith MBF.

Figure 25 shows the frequency response of the surface energies for both the core and shell exterior surfaces, i.e., respectively the surface separating the core from the shell and the surface separating the shell from air. The first six macrobasis functions for the core-shell structure are plotted in Figure 26 and Figure 27. Interesting enough, is the fact that on both core and shell interfaces the first six modes appear

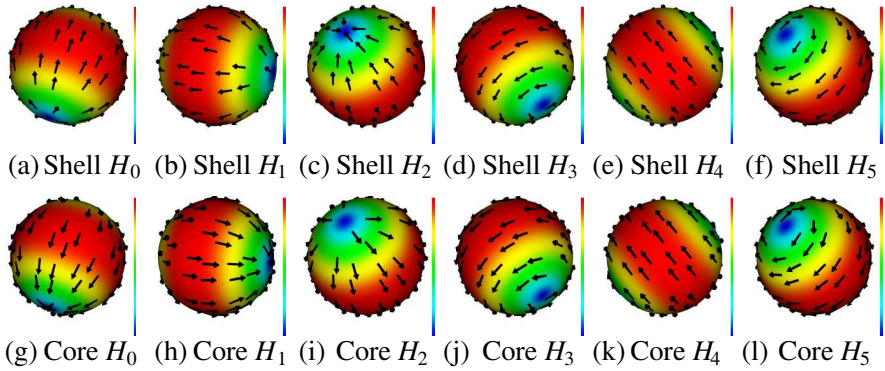

Figure 27. Core-shell. The real part of the tangential magnetic field due to the first six MBFs generated at $f = 190\,\text{THz}$. The $\mathcal{H}_i$ captions signify electrical and magnetic field representation of the ith MBF.

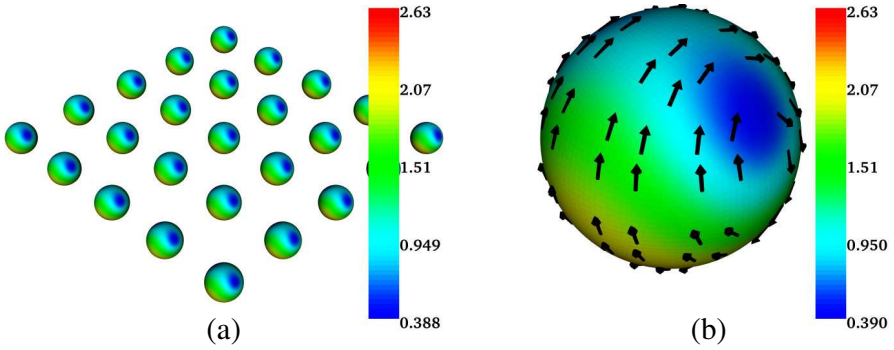

Figure 28. Core-shell. Real part of the tangential field solution of the 40×40 array in response to $\mathcal{E}^{inc} = \hat{x}e^{-\jmath k_0 \hat{z}\cdot\vec{r}}$. $\mathcal{E}/\mathcal{H}$ signifies the tangential electric/magnetic field. (a) $\mathcal{E}$ on the central 5×5 section. (b) $\mathcal{E}$ on the central element.

to consist of three simple magnetic dipole modes followed by another three electrical dipole modes. This, demonstrates the potential of the core-shell structure for realization of a DNG medium. The near field results for the 40×40 array are plotted in Figure 28 and Figure 29 where a combination of electric and magnetic modes is observed.

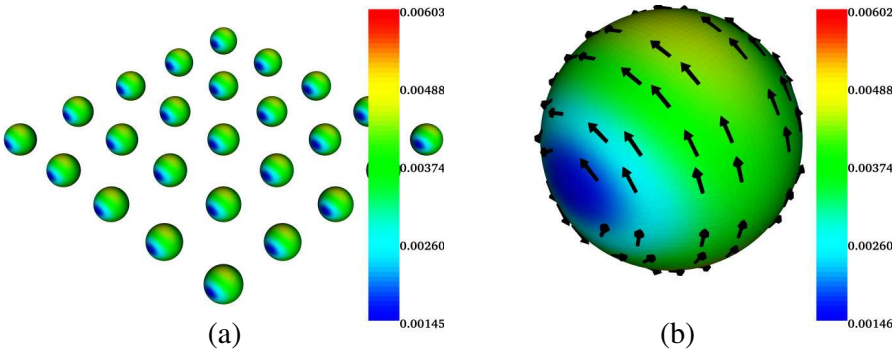

Figure 29. Core-shell. Real part of the tangential field solution of the 40×40 array in response to $\mathcal{E}^{inc} = \hat{x}e^{-\jmath k_0 \hat{z}\cdot\vec{r}}$. $\mathcal{E}/\mathcal{H}$ signifies the tangential electric/magnetic field. (a) $\mathcal{H}$ on the central 5×5 section. (b) $\mathcal{H}$ on the central element.

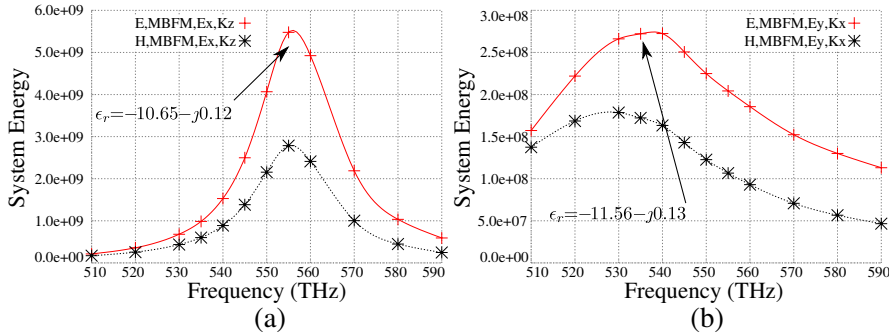

Figure 30. Plasmonic ring. The frequency response of the surface field energy on the 40×40 array. The E_x, E_y, K_x and K_z in the legend signify the polarization and propagation direction of the incident field. The arrow pointing to the peak of the curve indicates the actual value of the plasmonic ϵ_r around the resonance frequency. (a) $\mathcal{E}^{inc} = \hat{y}e^{-\jmath k_0 \hat{x}\cdot\vec{r}}$. (b) $\mathcal{E}^{inc} = \hat{x}e^{-\jmath k_0 \hat{z}\cdot\vec{r}}$.

3.5. Plasmonic Ring

As last example, we consider a plasmonic ring as the metamaterial building. It has a more complex configuration for computational modeling but provides unique features to control the underlying physics resonances. It has be shown that the behaviour of the loop structure can be successfully controlled by means of controlling the the aspect ratios associated with the geometry in the transverse and

vertical planes [21]. The plasmonic ring discussed here is a ring with internal radius of 20 nm, external radius of 40 nm and thickness of 30 nm. The lattice constant of the array structure is chosen to be equal to 300 nm. Similar to the plasmonic ellipsoid, the asymmetric geometry of the cell allows for the induction of different resonances by means of excitation of different electric field polarizations. As depicted in Figure 30, with the excitations given as $\mathcal{E}^{inc} = \hat{y}e^{-\jmath k_0 \hat{x}\cdot\vec{r}}$ and $\mathcal{E}^{inc} = \hat{x}e^{-\jmath k_0 \hat{z}\cdot\vec{r}}$, the structure shows resonances at around 540 THz and 555 THz respectively.

The first six macrobasis functions are listed in Figure 31. The first two modes have identical patterns but differ from each other by

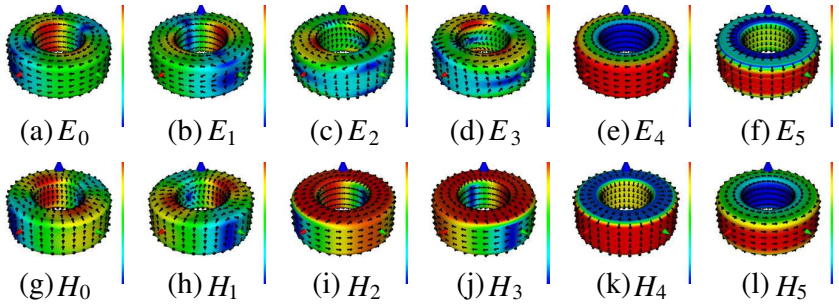

Figure 31. Plasmonic ring. The real part of the tangential field due to the first six MBFs generated for the array at $f = 550$ THz. The $\mathcal{E}_i$ and the $\mathcal{H}_i$ captions signify electrical and magnetic field representation of the ith MBF.

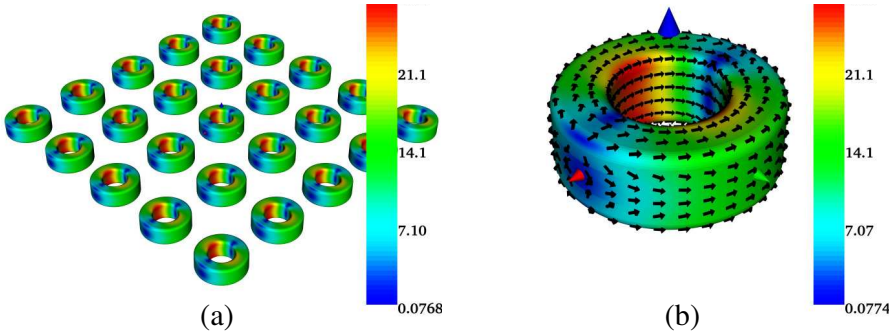

Figure 32. Plasmonic ellipsoid. Real part of the tangential field solution of the 40×40 array in response to $\mathcal{E}^{inc} = \hat{x}e^{-\jmath k_0 \hat{z}\cdot\vec{r}}$. $\mathcal{E}/\mathcal{H}$ signifies the tangential electric/magnetic field. (a) $\mathcal{E}$ on the central 5×5 section. (b) $\mathcal{E}$ on the central element.

a 90° rotation around $\hat{z}$ axis. The second two modes are also identical in pattern but differ by a 90° rotation around $\hat{z}$ axis. Nevertheless, the third and the fourth mode, respectively represent a magnetic and an electric dipole mode along $\hat{z}$. A glance at the near field results in Figure 32 and Figure 33 reveals that these solutions are very similar to the first macrobasis function as it is listed in Figure 31(a) and Figure 31(g). A similar analogy can be drawn between the near field solutions of Figure 34 and Figure 35 and the second macrobasis function listed in Figure 31(b) and Figure 31(h) where the electric field is polarized in the loop plane and along the loop arms while the magnetic field tends to spin around the arms of the loop.

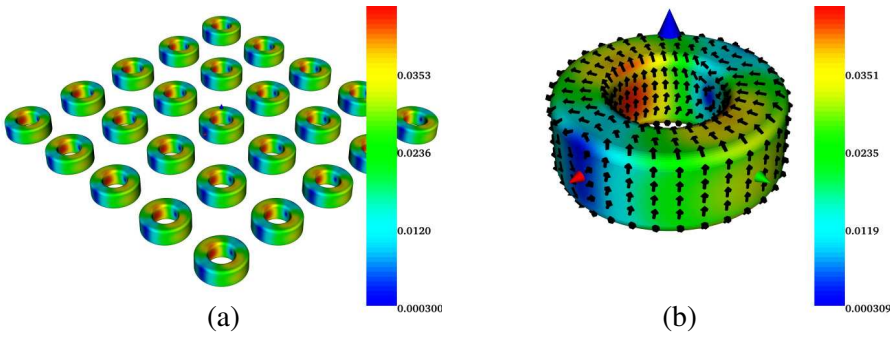

Figure 33. Plasmonic ellipsoid. Real part of the tangential field solution of the 40×40 array in response to $\mathcal{E}^{inc} = \hat{x}e^{-\jmath k_0 \hat{z}\cdot\vec{r}}$. $\mathcal{E}/\mathcal{H}$ signifies the tangential electric/magnetic field. (a) $\mathcal{H}$ on the central 5×5 section. (b) $\mathcal{H}$ on the central element.

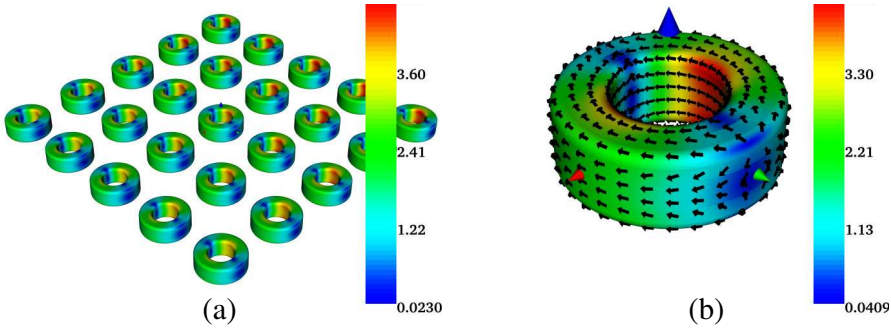

Figure 34. Plasmonic ellipsoid. Real part of the tangential field solution of the 40×40 array in response to $\mathcal{E}^{inc} = \hat{y}e^{-\jmath k_0 \hat{x}\cdot\vec{r}}$ at $f = 550\,\text{THz}$. $\mathcal{E}/\mathcal{H}$ signifies the tangential electric/magnetic field. (a) $\mathcal{E}$ on the central 5×5 section. (b) $\mathcal{E}$ on the central element.

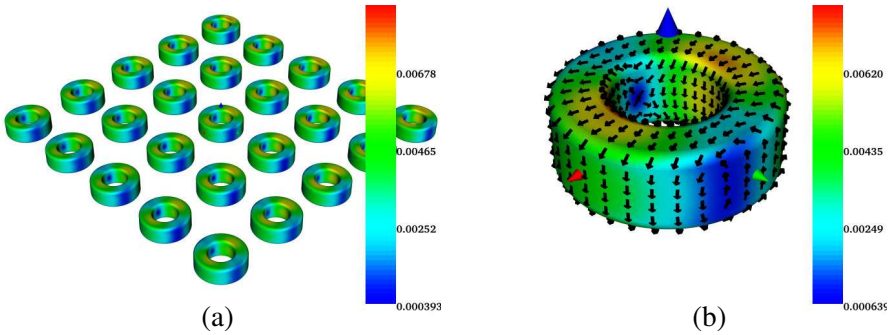

(a) (b)

Figure 35. Plasmonic ellipsoid. Real part of the tangential field solution of the 40×40 array in response to $\mathcal{E}^{inc} = \hat{y}e^{-\jmath k_0 \hat{x}\cdot\vec{r}}$ at $f = 550\,\text{THz}$. $\mathcal{E}/\mathcal{H}$ signifies the tangential electric/magnetic field. (a) $\mathcal{H}$ on the central 5×5 section. (b) $\mathcal{H}$ on the central element.

4. CONCLUSION

The macrobasis function approach discussed here is shown to be efficient and suitable for simulation of large metamaterial arrays made of complex building blocks. Using the proposed technique, a number of examples including arrays of dielectric and plasmonic spheres, ellipsoids, core-shells and plasmonic rings are solved. Aimed at large-area metamaterial arrays and considering the array redundancies inherent to the problem, the presented computational statistics indicate that the approach leads to significant computational advantages over the existing commercial solvers. Besides the efficiency, the method allows for gaining physical intuition to the nature of the problem due to the presence of the modal profile and the reduced solution that clearly reflects the contribution of various modes in the final solution. Like any other projection based technique, successful implementation of the the proposed MBFM relies on the proper choice of the projection space that is achieved by means of a systematic approach discussed in Subsection 2.4. Some unique physics involving the numerical results are discussed tha serve as a verification to the validity of the proposed methodology. The method can be easily applied to arrays with more than one type of building block while using composite building blocks can also help in improving the robustness and accuracy of the method.

ACKNOWLEDGMENT

This work is supported in part by the U.S. Office of Naval Research (ONR) MURI award Grant No. N00014-10-1-0942 and in part by U.S. Air Force Office of Scientific Research (AFOSR) Grant No. FA9550-10-1-0438. The authors would like to also acknowledge Masoud Rostami for his support and help in the design and verification of the spheroidal and core-shell building blocks. Last, but not least, our special thanks go to Soheil Saadat for helping with the CST simulations used throughout this work for the purpose of verification and benchmarking.

REFERENCES

1. Coifman, R., V. Rokhlin, and S. Wandzura, "The fast multipole method for the wave equation: A pedestrian prescription," *IEEE Trans. Ant. Prop.*, Vol. 35, No. 3, 7–12, Jun. 1993.
2. Seo, S. M. and J.-F. Lee, "A fast IE-FFT algorithm for solving PEC scattering problems," *IEEE Trans. Magn.*, Vol. 41, 1476–1479, May 2005.
3. Zhang, B., G. Xiao, J. Mao, and Y. Wang, "Analyzing large-scale non-periodic arrays with synthetic basis functions," *IEEE Trans. Ant. Prop.*, Vol. 58, No. 11, Nov. 2010.
4. Prakash, V. and R. Mittra, "Characteristic basis function method: A new technique for efficient solution of method of moments matrix equations," *Micro. Opt. Tech. Letters*, Vol. 36, Jan. 2003.
5. Hu, L., R. Mittra, and L.-W. Li, "Electromagnetic scattering by finite periodic arrays using the characteristic basis function and adaptive integral methods," *IEEE Trans. Ant. Prop.*, Vol. 58, 3086–3090, Sep. 2010.
6. Du, K. and R. Mittra, "Characteristic basis function method for iteration-free solution of large method of moments problems," *Progress In Electromagnetic Research*, Vol. 6, 307–336, 2006.
7. Maaskant, R., R. Mittra, and A. Tijhuis, "Fast analysis of large antenna arrays using the characteristic basis function method and the adaptive cross approximation algorithm," *IEEE Trans. Ant. Prop.*, Vol. 56, No. 11, 3440–3451, Nov. 2008.
8. Xiao, K., F. Zhao, S. L. Chai, J. J. Mao, and L.-W. Li, "Scattering analysis of periodic arrays using combined CBF/P-FFT method," *Progress In Electromagnetic Research*, Vol. 115, 131–146, 2011.
9. Rashidi, A., H. Mosallaei, and R. Mittra, "Scattering analysis of plasmonic nanorod antennas: A novel numerically efficient

computational scheme utilizing macro basis functions," *Journal of Applied Physics*, Vol. 109, 2011.

10. Stratton, J. A. and L. J. Chu, "Diffraction theory of electromagnetic waves," *Phys. Rev.*, Vol. 56, 99–107, Jul. 1939.
11. Ylä-Oijala, P. and M. Taskinen, "Application of combined field integral equation for electromagnetic scattering by dielectric and composite objects," *IEEE Trans. Ant. Prop.*, Vol. 53, No. 3, 1168–1173, Mar. 2005.
12. Taskinen, M., "On the implementation and formulation of electromagnetic surface integral equations," Ph.D. Thesis, 2006.
13. Solin, P. and K. Segeth, *Higher-order Finite Element Methods*, Chapman & Hall, 2004.
14. Graglia, R. D. and G. Lombardi, "Singular higher order complete vector bases for finite methods," *IEEE Trans. Ant. Prop.*, Vol. 52, No. 7, 1672–1685, Jul. 2004.
15. Johnson, P. B. and R. W. Christy, "Optical constants of the noble metals," *Phys. Rev. B*, Vol. 6, 4370–4379, 1972.
16. Stratton, J. A., *Electromagnetic Theory*, McGraw Hill, 1941.
17. Ahmadi, A. and H. Mosallaei, "Physical configuration and performance modeling of all-dielectric metamaterials," *Phys. Rev. B*, Vol. 77, 2008.
18. Ghadarghadr, S. and H. Mosallaei, "Coupled dielectric nanoparticles manipulating metamaterials optical characteristics," *IEEE Trans. Nanotechnol.*, Vol. 8, 585–594, Sep. 2009.
19. Ahmadi, A., S. Saadat, and H. Mosallaei, "Resonance and Q performance of ellipsoidal eng subwavelength radiators," *IEEE Trans. Ant. Prop.*, Vol. 59, No. 3, 706–713, Mar. 2011.
20. Biagioni, P., J.-S. Huang, and B. Hecht, "Nanoantennas for visible and infrared radiation," *Rep. Prog. Phys.*, Vol. 75, 2012.
21. Lipomi, D. J., M. A. Kats, P. Kim, S. H. Kang, J. Aizenberg, F. Capasso, and G. M. Whitesides, "Fabrication and replication of arrays of single- or multicomponent nanostructures by replica molding and mechanical sectioning," *ACS Nano*, Vol. 4, No. 7, 4017–4026, 2010.